V European Conference on Computational Fluid Dynamics
ECCOMAS CFD 2010
J. C. F. Pereira and A. Sequeira (Eds)
Lisbon, Portugal,14-17 June 2010

MULTIPHYSICS SPH FOR HARBOUR AND OCEAN ENGINEERING HYDRODYNAMICS

Christian Ulrich and Thomas Rung

Hamburg University of Technology (TUHH),
Inst. of Fluid Dynamics and Ship Theory (M-8),
Schwarzenbergstraße 95c, 21073 Hamburg, Germany
e-mail: christian.ulrich@tuhh.de, thomas.rung@tuhh.de

Key words: Smoothed Particle Hydrodynamics, Scouring, Water/Soil-Suspension, Harbour, Pipeline, Seabed Erosion

Abstract. *The paper reports on the SPH-modeling of water/soil-interactions. Emphasis is given to erosion simulations of seabeds and harbour grounds. The considered problems involve water/soil-suspensions. Accordingly, adequate models have been implemented into the massively-parallel hydrodynamic SPH-code* GADGET-$^{\mathrm{H}}2^{\mathrm{O}}$. *Validation examples refer to pressure and viscosity driven single- and multi-continua problems. Two marine-engineering applications devoted to erosions of the soil/water-interface are presented.*

1 INTRODUCTION

The interaction of water, soil and structures poses problems to different areas of marine and hydraulic engineering. In the area of ocean- and harbour-engineering, erosions close to platform legs, pipelines or quay walls represent unpleasant phenomena. In particular, scours may significantly weaken the structural support of the constructions and generate costly counter measures. While the formation of scours around offshore facilities usually follows their exposure to natural currents and waves, quay walls often suffer from flows induced by the ships' manoeuvering and propulsion devices. Scours are induced by large relative motions between the fluid and the soil. Such conditions usually lead to water/soil-suspensions which can be quite influential to the overall flow topology.

The Smoothed Particle Hydrodynamics (SPH) method discretises the continuum by means of particles rather than the spatial domain. The SPH-method is an ideal candidate to simulate ocean- and harbour-engineering problems, as it can handle the transient dynamics of multiple interacting continua featuring large relative motions. SPH-methods are mostly explicit by nature. They are however still associated to high computational expenses due to a virtually homogeneous discretisation of the continua and the time-step restrictions of a stable explicit integration scheme. Full-scale simulations of complex industrial flows at high Reynolds number can easily involve several ten-million particles and require massively-parallel simulations.

The present research aims to advance the modelling capabilities of the massively-parallel hydrodynamic SPH-code GADGET-$^{\mathrm{H}}2^{\mathrm{O}}$ [10] to compute engineering problems which involve the intreraction of fluid, soil and suspension layers. The GADGET-$^{\mathrm{H}}2^{\mathrm{O}}$-procedure is a modification of Springel's[9] cosmological TreeSPH-Code GADGET-2. GADGET-$^{\mathrm{H}}2^{\mathrm{O}}$ is seen to provide linear speed up for several hundred CPU-cores when applied to hydrodynamic flow simulations[10] using many ten-million particles. In the present study, fluids are assumed to be Newtonian and turbulence is modelled by means of an LES approach. The soil model considers the granular material as a fluid with a variable viscosity which is evaluated in line with the Mohr-Coulomb yield-stress criterium for cohesive or cohesionless materials. As opposed to this rather simple dry-soil model, the suspension model deserves more attention. A concentration based approach to mimic the stresses inside the fictitious suspension layer is introduced which is derived from a Chézy-relation between the shear stresses and the local flow velocity as proposed e.g. by Fraccarollo and Chapart[3].

The validation of the computational model refers to different pressure-driven and shear-driven flows of single phase-type as well as suspension flows. Applications included show the scour formation next to a quay wall during the unberthing manoeuver of a container vessel and the seabed erosion around a pipeline which is exposed to different regular waves.

The paper is structured as follows: In section 2, the employed governing equations and their respective finite approximations are described. Validation cases are presented in

section 3. Section 4 presents two application examples. Final conclusions are summarised in section 5.

2 COMPUTATIONAL MODEL

The section outlines the governing equations and their respective SPH-based approximations. Vectors and tensors are defined by reference to cartesian coordinates. The notation uses latin subscripts to identify particle locations and greek superscripts to mark cartesian tensor coordinates. The latin subscript i denotes to the focal particle whereas the subscript j refers to its neighbours. Mind, that Einstein's summation is employed over repeated Greek superscripts.

In accord with the SPH-formalism, the influence of neighbouring particles enters the framework of an integral representation by means of a compact-support kernel function W_{ij}, viz.

$$f(x_i) = \int f(x_j)\ \delta_D(x_i - x_j)\ dV \approx \int f(x_j)\ W_{ij}\ dV \approx \sum_{j=1}^{N} f(x_j)\ W_{ij}\ \frac{m_j}{\rho_j}\ .$$

The kernel function has to comply with the Delta-Dirac-function δ_D in the continuos limit, it should be symmetric and adhere to normalisation principle. It is assembled from the distance $r = |x_i^\alpha - x_j^\alpha|$ between two particles and drops to zero when the particle distance approaches the kernel length h. Accordingly, a standard cubic spline-kernel function is used in the present study

$$W_{ij} = W(r,h) = \frac{8}{\pi h^3} \begin{cases} 1 - 6\left(\frac{r}{h}\right)^2 + 6\left(\frac{r}{h}\right)^3 & 0 \le \frac{r}{h} \le \frac{1}{2}, \\ 2(1-\frac{r}{h})^3 & \frac{1}{2} < \frac{r}{h} \le 1, \\ 0 & \frac{r}{h} > 1\,. \end{cases} \tag{1}$$

Mind, that the kernel length can vary in GADGET-$^{\mathrm{H}}2^{\mathrm{O}}$, but is kept constant (2.4 times particle spacing) in the present research, as no benefits are expected from a variable smoothing length for incompressible fluids.

2.1 Conservation of Mass and Momentum

The transient evolution of the particle density follows from the continuity equation

$$\frac{D\rho_i}{Dt} = \sum_{j=1}^{N} \left[m_j (v_i^\beta - v_j^\beta) \right] \frac{\partial W_{ij}}{\partial x_i^\beta}\ , \tag{2}$$

where m denotes the particle mass and ρ marks the particle density. The velocity and the position of a particle refer to the vectors v^β and x^β, respectively.

The particles' momentum is governed by the Navier-Stokes equation, which is approximated using the following integral representation

$$\frac{Dv_i^\alpha}{Dt} = \sum_{j=1}^{N} \left[m_j \left(\frac{\sigma_i^{\alpha\beta}}{\rho_i^2} + \frac{\sigma_j^{\alpha\beta}}{\rho_j^2} \right) \right] \frac{\partial W_{ij}}{\partial x_i^\beta} + \frac{f_i^\alpha}{\rho_i} \,. \tag{3}$$

Here, f^α refers to a volumetric force and $\sigma^{\alpha\beta}$ denotes to the stress tensor. The latter is split into an isotropic pressure portion and a remainder

$$\sigma^{\alpha\beta} = -p\delta^{\alpha\beta} + \tau^{\alpha\beta} \,, \tag{4}$$

with the pressure p, the unit tensor $\delta^{\alpha\beta}$ and the stress tensor $\tau^{\alpha\beta}$.

2.2 Fluid Stress

For simple Newtonian fluids, $\tau^{\alpha\beta}$ represents the viscous stresses which depend on an isotropic viscosity μ^* and the strain-rate tensor $\epsilon^{\alpha\beta}$

$$\tau^{\alpha\beta} = \mu^* \epsilon^{\alpha\beta}. \tag{5}$$

Note, that $\epsilon^{\alpha\beta}$ corresponds to twice the conventional definition, viz.

$$\epsilon^{\alpha\beta} = \left[\frac{\partial v^\beta}{\partial x^\alpha} + \frac{\partial v^\alpha}{\partial x^\beta} \right] - \frac{2}{3} \left(\frac{\partial\, v^\gamma}{\partial\, x^\gamma} \right) \delta^{\alpha\beta}. \tag{6}$$

An SPH-approximation of (6) reads

$$\epsilon_i^{\alpha\beta} = \frac{1}{\rho_i} \sum_{j=1}^{N} \left[m_j (v_j^\beta - v_i^\beta) \right] \frac{\partial W_{ij}}{\partial x_i^\alpha} + \frac{1}{\rho_i} \sum_{j=1}^{N} \left[m_j (v_j^\alpha - v_i^\alpha) \right] \frac{\partial W_{ij}}{\partial x_i^\beta} \tag{7}$$

$$- \left[\frac{2}{3} \frac{1}{\rho_i} \sum_{j=1}^{N} m_j (v_j^\gamma - v_i^\gamma) \frac{\partial W_{ij}}{\partial x_i^\gamma} \right] \delta^{\alpha\beta}.$$

Turbulence is modelled by an eddy-viscosity model, thus the effective dynamic viscosity μ^* is composed from a viscosity μ and a turbulent viscosity μ_t

$$\mu^* = \mu + \mu_t. \tag{8}$$

The turbulent viscosity is obtained from a standard Smagorisky[8] model of a LES-approach as outlined by Gotoh et al.[4]

$$\mu_t = \rho (C_S h)^2 \, S^* \qquad \text{with} \qquad S^* = \sqrt{\epsilon^{\alpha\beta}\epsilon^{\alpha\beta}} \,, \tag{9}$$

where S^* represents a parameter related to the second invariant of the strain-rate tensor (6). The Smagorinsky constant is assigned to $C_S = 0.1$.

2.3 Hydrodynamic Equation of State (Pressure/Density-Relation)

The present effort is primarily concerned with incompressible fluids, e.g. water and water/soil-suspensions. The computation of the pressure field in an incompressible fluid poses a challenge to classical SPH-simulations using an explicit time-stepping technique. In the present study, the flow is considered weakly compressible. Accordingly, Tait's pressure-density relation[2] with the generally recommended exponent $\gamma_T = 7$ is used

$$p = \left[\left(\frac{\rho}{\rho_0} \right)^{\gamma_T} - 1 \right] p_0 \ . \tag{10}$$

Following to Monaghan[6], equation (10) is applicable in weakly-compressible flows, if the reference pressure p_0 is assigned to a slightly small value. This manipulation results in an enhanced compressibility but avoids both, numerical instabilities and prohibitively small time steps. The compressibility is deemed negligible, if the density variations are smaller than 1%. Since density variations scale with the square of the Mach number, virtually incompressible flows are obtained if the entire flow field adheres to $M \leq 0.1$. A frequently employed pressure/speed-of-sound relation reads

$$\gamma \, \frac{p_0}{\rho_0} = c^2 \ , \tag{11}$$

where c refers to the speed of sound and ρ_0 marks the initial density value. To satisfy the low Mach-number constraint, the speed of sound and the reference pressure are approximated by

$$c = 10 \ v_{max} \ \ (\text{thus} \, M \leq 0.1) \qquad \rightarrow \qquad p_0 = \frac{100 \ v_{max}^2 \ \rho_0}{\gamma} \ . \tag{12}$$

The approach (10-12) is known to display disturbances for flows featuring negligible dynamics (e.g. for hydrostatic problems). Accordingly, the XSPH[6] approach is used to address these issues

$$\frac{dx_i^\beta}{dt} = v_i^\alpha - \epsilon_{xsph} \sum_{j=1}^{N} \frac{m_j}{\rho_j} (v_j^\beta - v_i^\beta) W_{ij}. \tag{13}$$

In the present study, the smoothing factor is set to $\epsilon_{xsph} = 0.1$.

2.4 Soil Model

The continuity and momentum equations are conveniently employed to also evaluate the soil motion. Hence, the soil particles are treated as a viscous material with a variable viscosity. For the examples included, the soil-viscosity adheres to the Mohr-Coulomb yield-stress criterion for granular materials

$$\mu = \frac{\mathcal{C} + p \cdot \sin\Phi}{S^*} < \mu_{max} \ . \tag{14}$$

In equation (14) Φ denotes the internal angle of friction and $\mathcal{C}$ refers to the cohesion. Equation (14) gets singular when the strain-rate parameter becomes very small. Therefore, an upper threshold value is defined for the soil-viscosity. Accordingly, an upper value of $\mu_{max} = 5000$Pa s seems to be a fair compromise between computational and physical considerations. More elaborate (strain based) soil models – e.g. the Drucker-Prager models – can be employed, when the attention is devoted to the pure soil.

2.5 Water/Soil-Suspension Model

The present suspension model aims to accurately mimic the influence of viscous effects inside a suspension layer nested between the water and soil regions. The evolution of the liquid and granular particles is obtained from the continuity and momentum equations. The fluid is considered to be Newtonian and the viscosity of the soil-phase is modelled in line with the Mohr-Coulomb yield-stress criterium as described in section 2.4. Particles which reside inside a fictitious suspension-layer are assigned to a viscosity that is derived from a Chézy-relation between the stress and the local flow velocity, along a route outlined by Fraccarollo and Chapart[3]

$$\mu_c^* = \frac{\rho_s \, C_f \, (v^\alpha v^\alpha)}{S^*} + \mu_t \tag{15}$$

In eq. (15) the soil density is denoted by ρ_s and C_f refers to the friction coefficient of the Chézy-relation. Fraccarollo and Chapart[3] recommend C_f-values in a range of 0.007 to 0.03. In the present research, a value of $C_f = 0.01$ is adopted. To bridge between the soil, suspension and fluid regimes, three different regions are defined, depending on the local volumetric soil concentration $\tilde{c}_{soil}$. The Chézy-relation viscosity μ_c^* is assigned to the central region with $0.3 < \tilde{c}_{soil} < 0.6$. A linear interpolation between μ_c^* and the liquid-phase viscosity μ_l^* is applied in the wetted-regime ($\tilde{c}_{soil} \leq 0.3$). An analogue approach is used for the dry regime ($\tilde{c}_{soil} \geq 0.6$), viz.

$$\mu_{susp}^* = \begin{cases} \mu_l^* + \frac{\mu_c^* - \mu_l^*}{0.3} \tilde{c}_{soil} & \tilde{c}_{soil} \leq 0.3 \\ \mu_c^* & 0.3 < \tilde{c}_{soil} < 0.6 \\ \mu_c + \frac{\mu_s^* - \mu_c^*}{1-0.3} (\tilde{c}_{soil} - 0.6) & \tilde{c}_{soil} \geq 0.6 \end{cases}, \tag{16}$$

2.6 Boundary Conditions

The present effort utilizes rather simple wall-boundary conditions. Boundary particles are flagged and their locations are frozen. In conjunction with stationary walls, the latter is realized by imposing zero acceleration. The wall particles participate as regular particles in all calculation steps. Note, that their density and pressure might change and that the wall-particles are also capable of inducing shear forces. The walls can represent fixed fluid as well as soil including the appropriate physical characteristics.

Many engineering applications are based on moving walls. Supplementary to the above described wall model, the wall-velocities are assigned to the dedicated value. The actual wall position can be evaluated from an integration of the prescribed wall velocities, or defined by a compliant direct specification.

2.7 Time Integration

The SPH-approach facilitates an approximation for spatial derivatives. A modified leap-frog scheme is used to advance the solution in time. Accordingly, two time-shifted discretisations – referred to as drift and kick positions – are employed for the velocity. The density evolution is obtained from an approach that uses half the time step of the momentum scheme and alternates between a drift-step, which refers to an analytical solution to the continuity relation

$$\frac{D\rho}{Dt} = -\rho \frac{\partial v^\alpha}{\partial x^\alpha} \ ,$$

and a kick-step employing equation (2). The integration of the momentum equation follows a leap-frog approach, where the velocities at the drift positions are used to determine the stress tensor for the kick-step and will be corrected henceforth. The time step is restricted by multiple Courant conditions, viz.

$$\Delta t \leq \ 0.2 \ \min \left[\sqrt{h/|f^\alpha|}, h/c, \rho h^2/\mu^* \right] \ .$$

3 VALIDATION

3.1 Pressure Driven Fluid Flow

The collapsing water column experiment presented by Martin and Moyce[5] is used for the validation of pressure driven flows. The initial water column has a height which is twice as large as its width. The flow is considered to be laminar. The evolutions of the columns width and height during the collapse are compared to experimental data[5] and a numerical Eulerian Volume of Fluid (VOF) reference solution[7]. Figure 1 displays the initial set-up. The fluid column is modelled in 2D with a total number of 800 particles. The particle spacing is assigned to 0.0028575m and yields the initial geometry of the experiment.

The results of the dambreak test case are presented in figure 2. Despite the coarse discretisation, the results obtained by GADGET-$^{\mathrm{H}}2^{\mathrm{O}}$ show a fair predictive agreement with the numerical reference, both for the width and the height. The prediction of the column's height also matches the experimental results. A deviation from the experiment can be observed for the column's width. Such deviations have been observed in other author's validation studies[7,11] as well and may be due to several aspects of the experiments that are not captured by simulations, like e.g. difficulties in tracking the surge's front, bed friction or parts of the gate membrane influencing the flow.

Figure 1: Schematic sketch of the initial set-up for the collapsing water column.

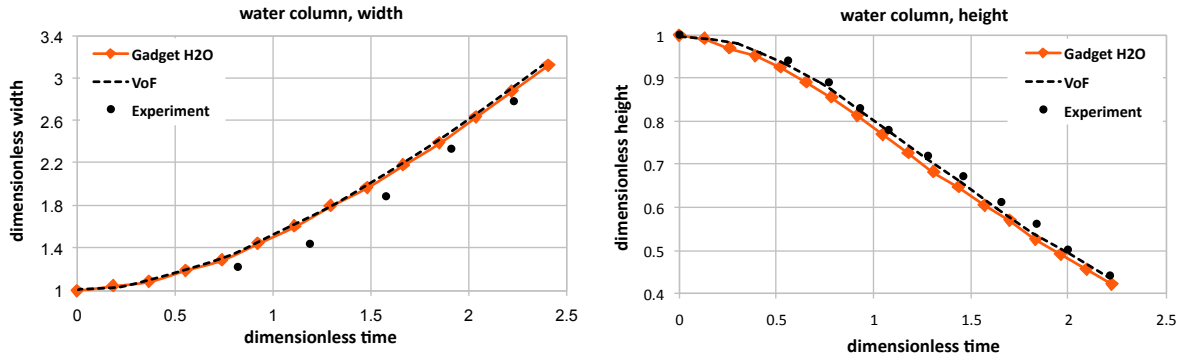

Figure 2: Evolution of collapsing water column by means of width (left) and height (right). SPH-predictions using GADGET-$^{H}2^{O}$ are represented by the red line and rhombi. Experimental[5] data is marked by black dots while the numerical reference solutions based on Eulerian VOF[7] are represented by the dashed black lines.

3.2 Shear Driven Fluid Flow

SPH-methods are traditionally inviscid. Hence, the viscous flow model and the implementation of viscous boundaries should be validated. Moreover, attention should be given to flows driven by viscous forces which are introduced along the walls. Accordingly, a laminar axisymmetric Couette flow is simulated. As diplayed in figure 3, the example refers to two co-axial cylinders with the radii R_1 and R_2 which are rotating with the angular velocities ω_1 and ω_2. The rotating walls induce a rotating shear-flow. The analytical solution for the circumferential velocity v_φ reads

$$v_\varphi(r) = \frac{A}{2} r + \frac{B}{r} \,, \tag{17}$$

where A and B depend on the geometry and the rotation of the cylinders. Results are compared for the normalized circumferential velocity

$$\tilde{v}_\varphi = \frac{v_\varphi(r) - v_\varphi(R_1)}{v_\varphi(R_2) - v_\varphi(R_1)} \quad \text{and} \quad \tilde{r} = \frac{r - R_1}{R_2 - R_1}.$$

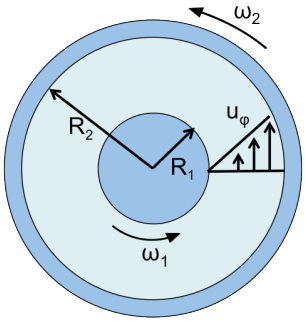

Figure 3: Schematic sketch of the axisymmetric Couette flow. A shear driven velocity profile will develop between two cylinders rotating with the angular velocities ω_1 and ω_2.

The radii of the two cylinders are assigned to $R_1 = 0.15$m and $R_2 = 1$m. Two rotation rates have been simulated. The more simple case refers to $\omega_1 = \omega_2 = 10$Hz, the more challenging case pertains to $\omega_2 = 10$Hz and $\omega_1 = 0$. A total number of 4769 particles has been used for the 2D discretisation of the fluid with a particle spacing of 0.025m. To supress instabilities and turbulence, the dynamic viscosity is set to $\mu = 1000$Pa s.

The simulation results after 10 rotations of the outer wall are presented in figure 4. A satisfactory agreement between the numerical and analytical velocity profiles can be observed. Minor deviations occur next to the cylinder walls.

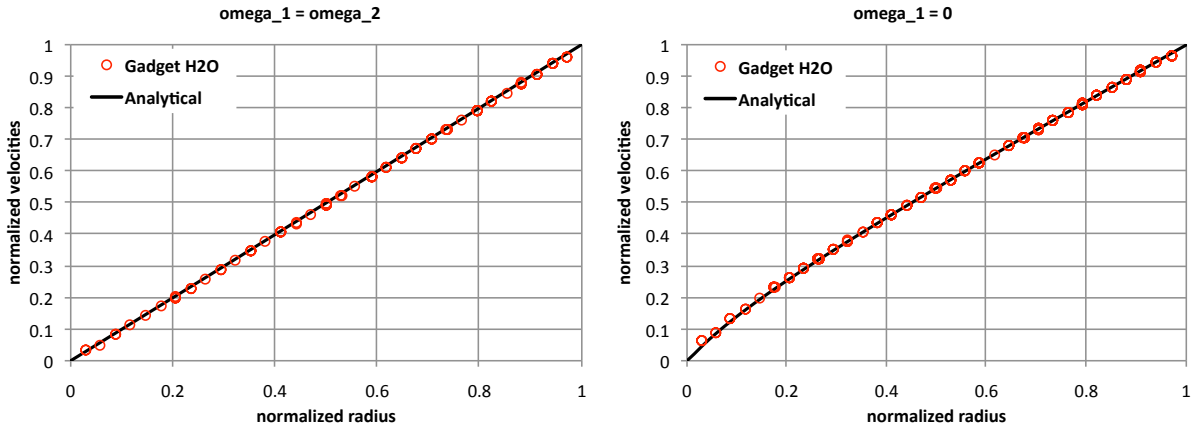

Figure 4: Predicted and analytical velocity profiles for the axisymmetric Couette-Flow (Left: $\omega_1 = \omega_2 = 10$Hz. Right:$\omega_2 = 10$Hz and $\omega_1 = 0$); The black line represents the analytical solution while the numerical results are marked with the red circles.

3.3 Pure Soil Motion

A collapsing sand column is simulated for the validation of the soil model as illustrated in figure 5. The present example refers to a cohesionless soil with an internal friction $\Phi = 45°$. The soil density reads $\rho = 1600\text{kg/m}^3$ and a threshold viscosity of $\mu_{max} = 12$kPa·s

has been used. Figure 5 shows the column before and after the collapse. The initial 3D column has a height of 0.1m and a squarish base with a width of 0.03m. The particle spacing is 0.005m.

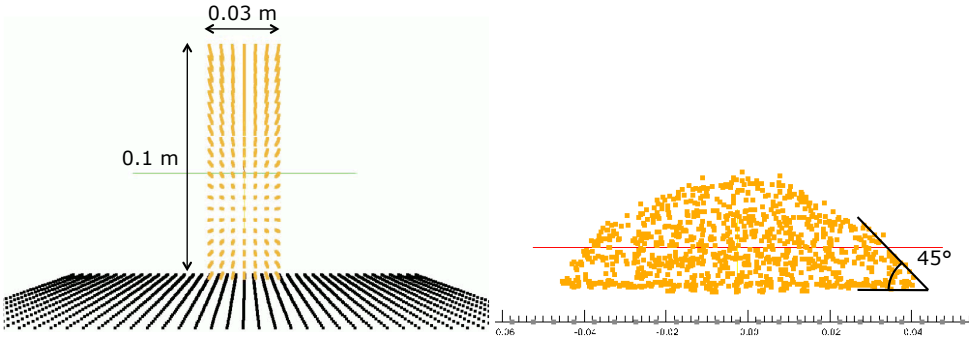

Figure 5: Collapsing sand column; Left: initial configuration, Right: End configuration. The specified internal angle of friction 45° can be found as the slope angle at the forming debris cone.

After the collapse, the specified internal angle of friction can be found as the resulting slope angle indicating a correct implementation of the material model. The final cone geometry is displayed in figure 5. Mind, that the soil is modelled as a fluid and thus continues to creep once the internal friction angle has been reached on the forming debris cone. The employed threshold viscosity significantly influences the creeping behaviour of the cone and should not be chosen too small.

3.4 Water/Soil-Suspension Flow

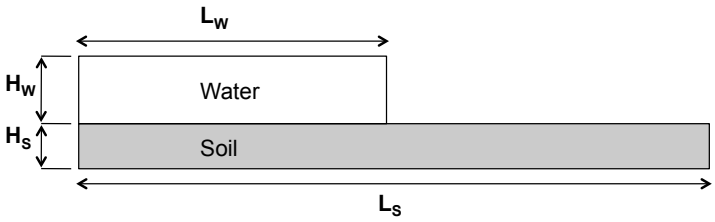

Figure 6: Schematic sketch of the Louvain erosional dambreak experiment[3].

The Louvain erosional dambreak experiment presented by Fraccarollo and Chapart[3] is used to validate the suspension model. Figure 6 depicts the basic set-up. A water column with a length L_w and height H_w is situated above a soil bed with the extensions L_s and H_s. The collapse of the water column induces a surge leading to erosions of the soil. A suspension layer forms between the pure soil and fluid whose evolution has been tracked in the experiments. The two-dimensional case is modelled with the dimensions $L_w = 1$m, $H_w = 0.1$m, $L_s = 2$m, $H_s = 0.6$m and a particle spacing of 0.005m leading to 4221 water

particles and 4812 soil particles. The soil density ρ_s and the water density ρ_w follow the relationship $\rho_s = 1.54\rho_w$. The threshold soil viscosity is set to $\mu_s = 5000$Pa s.

Figure 7 shows the evolution of the three phases for the experiment and the simulations at different points in time. Two simulations are considered in the comparison. The first simulation refers to the application of the Chézy-suspension model (16) described in section 2.5. The second simulation is performed without a special treatment of the ficticious suspension layer. Here, the local flow properties are obtained from the standard kernel operations using the neighbouring particle properties.

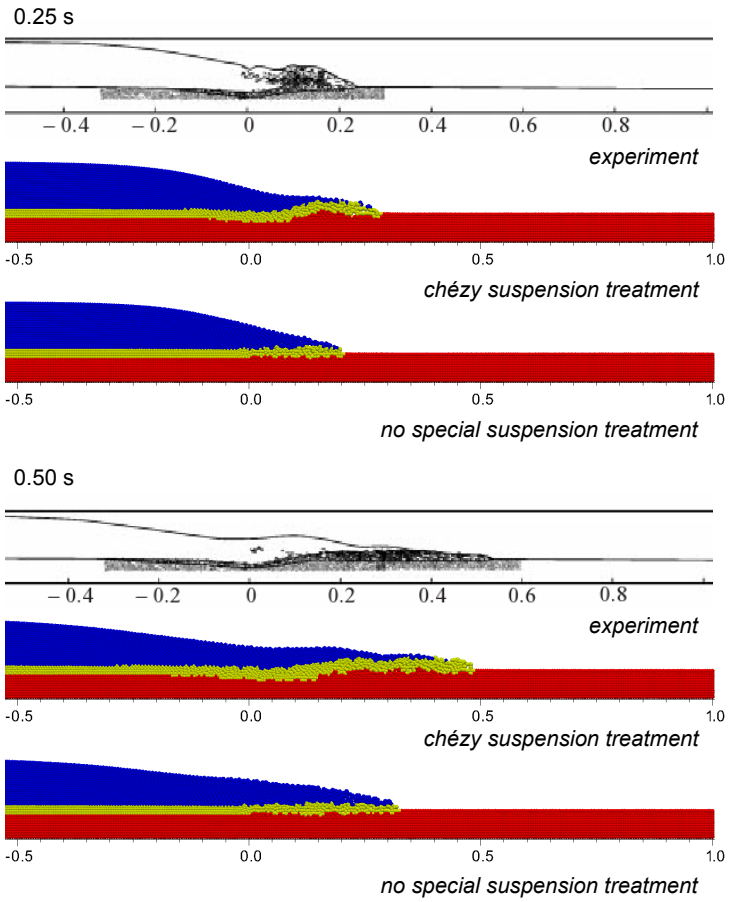

Figure 7: Snapshots of the Louvain experiment[3] and simulations. The first picture of each point in time refers to the experiment, the second to predictions using the Chézy relation (16), while the third pictures show a simulation without any special treatment of the suspension layer. The experimental snapshots show estimated interfaces between the soil, suspension and water. For the simulation, the three different phases are coloured: Blue represents pure water, red pure soil and yellow refers to the suspension layer.

Figure 7 shows an encouraging agreement for the evolution of the different interfaces between the experiment and the simulations with Chézy-suspension treatment. As opposed to this, the predictive accuracy significantly deteriorates in conjunction with the

standard approach. The propagation velocity of the surge front is obviously to slow for the standard approach and much faster for the Chézy-suspension treatment. The related erosion is more pronounced for the Chézy-suspension treatment and captures a thickening of the suspension layer in line with the experiments. Moreover, results obtained from the advanced suspension model confirm the experimental observation, that the fluid phase lags behind the suspension layer at later stage.

Figure 8 depicts the predicted interfaces using the Chézy-suspension treatment in comparison to experimental observations. The simulation matches the measured interface-contours quite well. The surge front of the suspension layer shows some deviations which may be due to the discretisation or the parameters of the suspension model. The overall agreement is nonetheless satisfactory and the computational model seems to be able to capture the principal phenomena of an erosional dambreak.

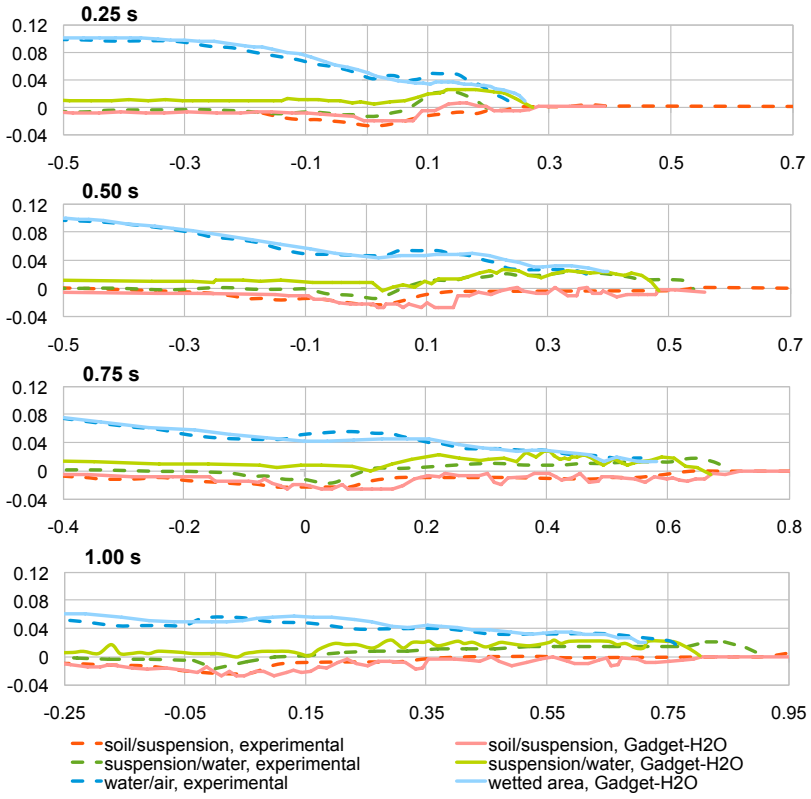

Figure 8: Evolution of phases interfaces of the Louvain dambreak; Comparison of measured and predicted interfaces using equation (16) for different points in time.

4 APPLICATIONS

4.1 Ship Unberthing Manoeuver

This first application refers to the scour generation during the unberthing manoeuver of a container ship. In particular, the flow induced by transverse thrusters can lead to scouring, especially if the ship is located close to a quay wall which deflects the jet towards the harbour bed. Such erosions can significantly weaken the quay-wall support and lead to cost expensive counter measures. Figure 9 illustrates the basic scouring mechanism. The present example shows an simplified 3D simulation of a 8200 TEU container vessel. The considered ship has a length of 334m, 38m width and a scantling draft of 14.5m. The installed transvers thruster delivers 2.5MW.

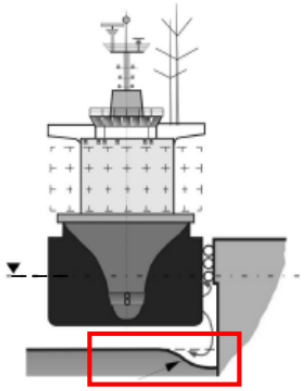

Figure 9: Sketch of scouring due to a deflected transverse bow thruster jet.

A 2D discretisation of the bow thruster frame geometry is created where the particles are a located on a regular grid with particle spacing of 0.2m. To derive a 3D model, the frame geometry is expanded to a length of 10m which also includes a thruster tunnel in the center. The tunnel diameter measures 3m. Figure 10 shows the particle discretisation and the geometric properties of the considered ship section.

As displayed in figure 10, the ship section is embedded into an idealized harbour basin of 80m length, 24m width and 16.6m depth. The configuration leads to 2.1m water between the ship's bottom and the 2.2m thick harbour bed. The ship's centre line is located 19m from the basin boundary which represents the quay wall. Including the ship model, the dimensions lead to $5.2 \cdot 10^6$ particles. The complete ship/harbour-model consists of four different particle types, as indicated by different colours in figure 10. The blue particles refer to fluid, the yellow ones represent the soil while the red and grey particles indicate boundaries according to section 2.6. The basin bottom (red) is modelled with fixed sand soil particles while the other boundaries use fixed fluid particles. The ship section (dark grey) is also modelled by such boundary particles but will be moved throughout the simulation.

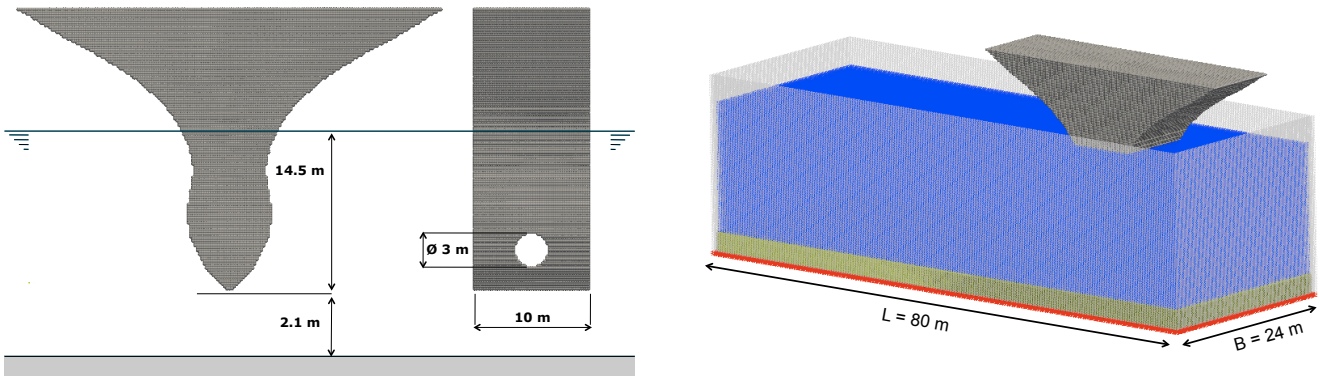

Figure 10: Simplified ship/harbour-model; The considered ship section is coloured in dark grey, water particles are marked blue, soil is represented in yellow. The soil boundaries are marked red while the water boundary particles are coloured in light grey.

The ship's motion during the simulation is approximated by taking into account its mass, estimated added mass, underwater lateral area and the thrust induced by the transverse thruster. According to Brix[1], the thruster's jet velocity v_T can be approximated by a simple momentum theory

$$v_T = \sqrt[3]{\frac{2P_T}{\rho A_T}}, \tag{18}$$

with the fluid density ρ, thruster's power P_T and cross-sectional area A_T. The thrust is related to the power and jet velocity

$$v_T = \frac{2P_T}{T} \ . \tag{19}$$

For the present case, a thrust of $6 \cdot 10^6$N is obtained from the power and tunnel area. While the ship is moving sideways, it will produce a drag that is obtained from

$$F_D = 0.5\rho v_s^2 C_D A_s \ . \tag{20}$$

The drag-force coefficient is estimated by $C_D = 1$, the underwater lateral area refers to $A_S = 4000\text{m}^2$ and the ship velocity is marked by v_s. The ship motion is computed from the integration of the momentum relation

$$(M_s + M_h)\frac{Dv_s}{Dt} = F_D - T. \tag{21}$$

Equation (21) takes into account a ship mass of $M_s = 10^8$kg. The added mass is roughly estimated to have the constant value $M_h = M_s$.

The jet velocity v_T is imposed on the fluid particles located within the thruster tunnel. For each time step and each particle in the domain of interest, an acceleration is calculated

which ensures that the particle reaches the desired jet velocity according to equation (18) within one time step.

Figure 11 shows vector plots of the jet velocity in the centre section at different points in time. It can be observed that the jet reaches the quay wall after approximately 5s.

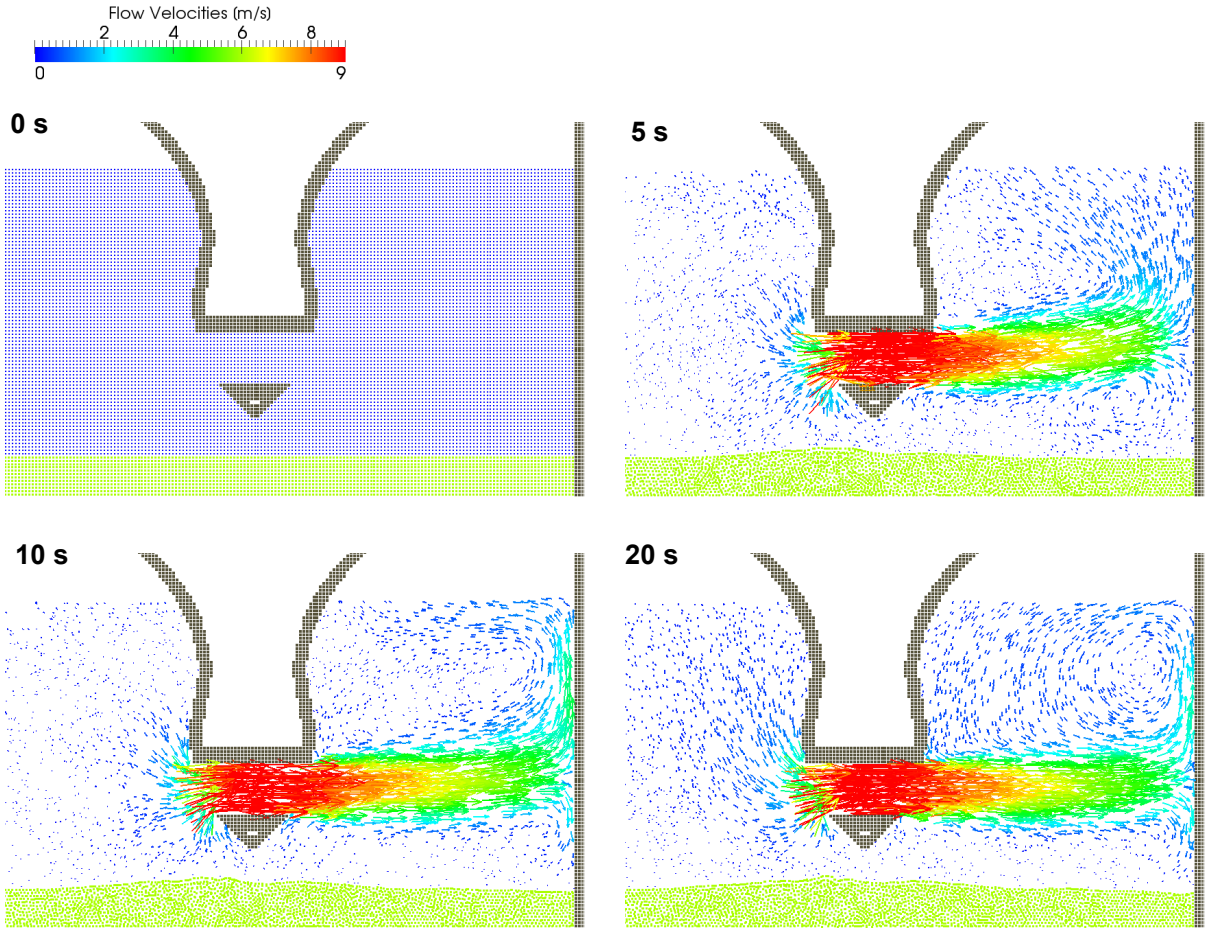

Figure 11: Evolution of the thruster jet. The vector arrows are scaled and coloured accordingly to the velocity values.

Due to the thruster suction, erosion occurs right from the beginning of the simulation beneath the ship. The formation of vortices can be observed as the jet exits the thruster leading to some minor erosion phenomena. The primary erosion of the harbour bed is initiated when the jet hits the quay wall. The transient evolution of the scour depth at a position in the center plane through the tunnel at 0.5 m from the wall is plotted in figure 12.

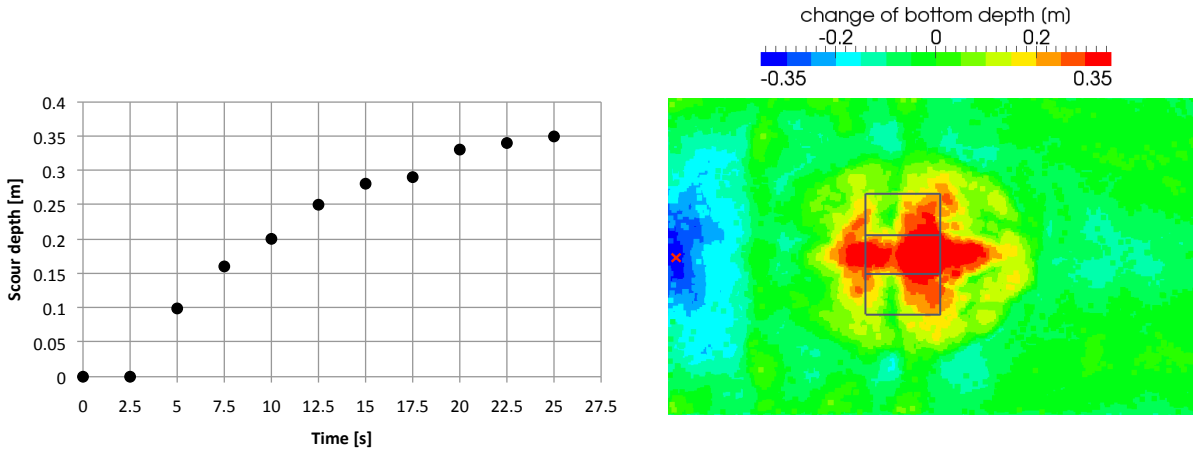

Figure 12: Left: Evolution of the scour depth at a position in the center plane through the tunnel at 0.5 m from the wall. Right: Harbour bed topography after 20 s. The red cross refers to the measuring point for the scour depth (plot left). The grey lines show a cut through the ship section in the thruster centre.

A scour of approximately 0.35m depth can be observed next to the wall after only 25s as illustrated in figure 12. The figure also shows the harbour bed topography. Aside the main scour next to the wall, some smaller bottom lowering can be observed around the section. The out-washed sediment accumulates below the section.

A real unberthing manoeuver would probably take longer and yield a deeper scour. It cannot be expected that the scour will completely disappear during the next berthing. Moreover, the ship draft and size and the propulsion unit will also have strong influences on the scour generation. Therefore, comprehensive simulation series should be carried out to assess the long-term evolution of the harbour-bed erosion and the resulting impact on the structural quay support.

4.2 Seabed Erosion around Pipeline

The second application example studies the seabed erosion next to a pipeline which is exposed to an alternating current induced by regular shallow water waves. The basic geometric properties are shown in figure 13. The pipeline diameter D is set to 1.2m with a trenching depth of 0.15m and a still-water level of 3.0m. The example refers to an idealized near-shore pipeline.

The case is modelled in 2D using a 0.05m particle spacing. The simulated basin has a wetted length of 40m with a beach on the one end and a wave-maker paddle on the other end. The total number of particles is 45754. Two different waves are considered. The wave properties are listed in table 1. The length of the first wave is set to 40m, which seems to be the longest applicable length due to the basin dimensions. The height of the first wave is 0.325m. The second, steeper wave has a length of 10m and a height of 0.75m. We refer to the waves as "long wave" and "short wave". The waves are generated by flap motion of the paddle, which has its pivot point at the same height as the water/soil-interface.

This leads to an excitation of the complete water column.

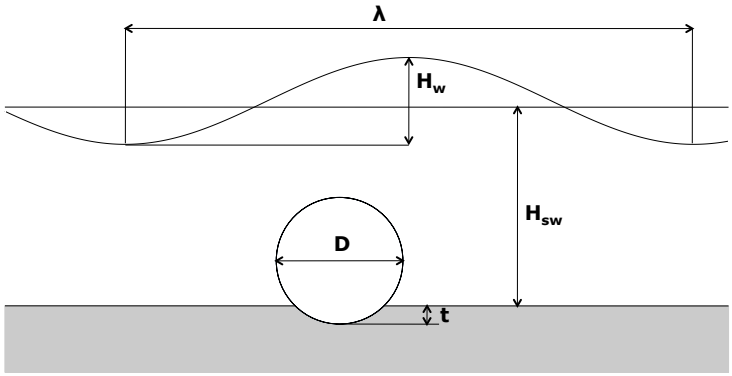

Figure 13: Schematic sketch of the pipeline exposed to regular waves.

Depending on the wave-induced variation of the water level, the flow topology around the pipeline will not be perfectly mirrored for the wave crest or through situation. Due to stronger blockage effects, the current will be stronger if the through is situated above the pipeline. Such effects grow with an increasing wave height. Figures 14 and 15 show the flow topology around the pipeline for the crest and through situations of both waves. Vectors are scaled in their length and coloured corresponding to the velocity magnitude. As illustrated by figure 14, the flow topology insignificantly changes (besides its orientation) for the crest or through of the long wave. Dead-water zones can be observed on both sides of the pipeline. Due to the flow symmetries, symmetric erosions are expected. The flow topology looks different if the pipeline is exposed to the short wave (cf. figure 15). Due to the smaller blockage, the maximum flow velocities are much slower if the crest is situated above pipeline than at the through point. The topology does not show a mirrored characteristic for the two situations. The flow field shows a more rotational structure due to the shorter wave length and larger wave height. The dead water zones on both pipeline sides are much larger than for the long wave. For the through point, the dead water at the upstream side of the pipeline is smaller than for the crest. Hence, asymmetric erosions are likely to be formed.

	long wave	**short wave**
length λ **[m]**	40	10
height h **[m]**	0.325	0.75
period T **[s]**	7.5	2.5

Table 1: Wave parameters.

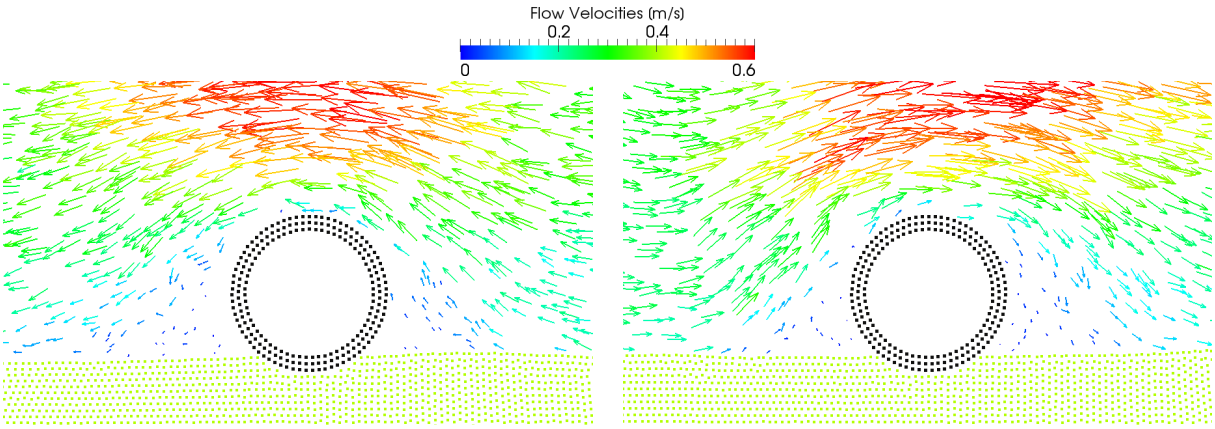

Figure 14: Flow topology around the pipeline for the long-wave scenario; vectors are scaled according to the velocity magnitude. Left: wave through located right above the pipeline – Right: wave's crest located above the pipeline. An almost perfectly mirrored flow topology can be observed.

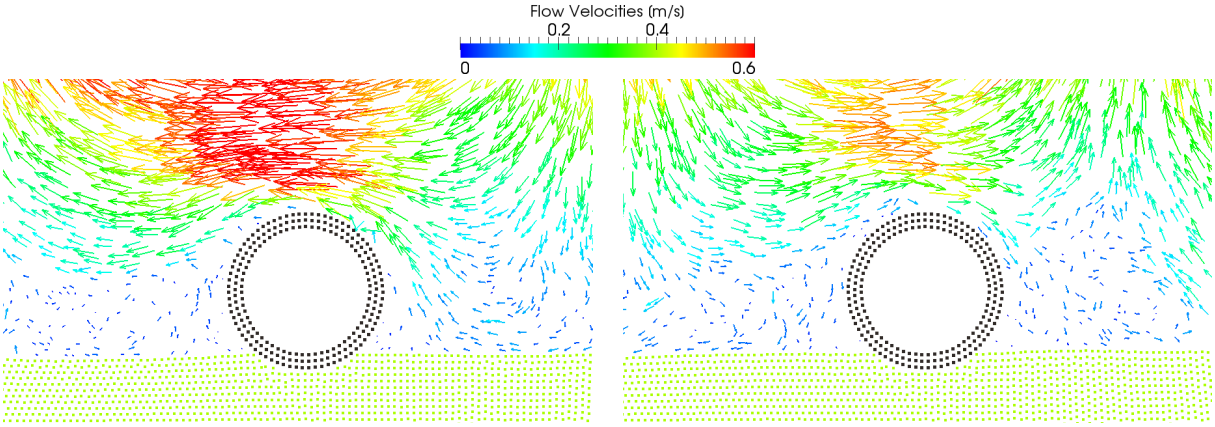

Figure 15: Flow topology around the pipeline for the short-wave scenario; vectors are scaled according to the velocity magnitude. Left: wave through located right above the pipeline – Right: wave's crest located above the pipeline. Unlike for the long wave, the flow topology is completely different for the two points in time.

Results for the seabed erosion are displayed in figure 16. The figure shows soil levels at the initial state and after 25 wave periods both for the short and the long wave. The wave is propagating from the left side. It can clearly be observed, that a symmetric erosion is predicted for the long-wave scenario. This corresponds well to the flow topology presented in figure 14. At both sides, soil accumulations form at a certain distance aside the pipeline. This is caused by sediments which are convected with the fluid phase untill the flow recirculates. For the short-wave scenario, a pothole is generated at the left side of the pipeline while a soil accumulation forms at its right. The latter effect is the same (but not as strong) as for the long wave. The left-side scour can be explained by the attenuated near-ground convection for the wave crest. Hence, the pothole is always generated on the

pipeline's downstream side. It can grow and will not be filled with sediment.

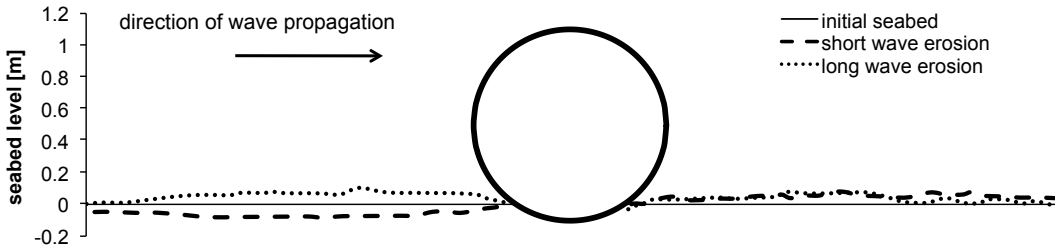

Figure 16: Evolution of the seabed contour. The solid line represents the initial condition. The dashed line refers to the erosion after the seabed has been exposed to 25 periods of short waves while the dotted line shows the erosion due to 25 long waves.

5 CONCLUSIONS

The paper reports on a multiphysics SPH-model to study water/soil-interaction. Emphasis is given to an accurate simulation model of the suspension layer. The latter is significant for the overall predictive performance of a water/soil-simulation when large relative velocities occur at the interface, e.g. during the generation of potholes. An improved concentration-based water/soil-suspension model for the viscous stress inside the suspension layer has been presented as a supplement to traditional SPH-formulations for the liquid and granular phase. The model has been successfully validated and returns promising predictive benefits.

Two applications for the pothole generation have been presented which indicate the prospects of the GADGET-$^{\mathrm{H}}2^{\mathrm{O}}$ SPH-procedure for the simulation of industrial ocean- & harbour-engineering applications. The procedure will be supplemented by more advanced propulsor models to perform further unberthing simulations.

6 ACKNOWLEDGMENT

The authors would like to thank the German Research Foundation (Deutsche Forschungsgemeinschaft, DFG) for supporting the project. The present work forms part of the Research Training Group Ports for Container Ships of Future Generations: Interaction of Ship, Fluid, Structure and Soil (GRK 1096) at the Hamburg University of Technology.

REFERENCES

[1] J. Brix, editor. *Manoeuvring Technical Manual*. Seehafen Verlag, 1993.

[2] R. H. Cole. *Underwater Explosions*. Princeton University Press, 1948.

[3] L. Fraccarollo and H. Chapart. Riemann wave description of erosional dam-break flows. *Journal of Fluid Mechanics*, 461:183–228, 2002.

[4] H. Gotoh, S. Shao, and T. Memita. SPH-LES Model for Wave Dissipation using a Curtain Wall. *Anual Journal of Hydraulic Engineering*, 47:397–402, 2003.

[5] J. C. Martin and W. J. Moyce. Part IV. An Experimental Study of the Collapse of Liquid Columns on a Rigid Horizontal Plane. *Philosophical Transactions of the Royal Society A*, 244(882):312–324, 1952.

[6] J. J. Monaghan. Simulating Free Surface Flows with SPH. *Journal of Computational Physics*, 110:399–406, 1994.

[7] J. Sauer. *Instationär kavitierende Strömungen - Ein neues Modell, basierend auf Front Capturing (VoF) und Blasendynamik*. PhD thesis, Fakultät für Maschinenbau, Universität Karlsruhe, 2000.

[8] J. Smagorinsky. General circulation experiments with the primitive equations. I. The basic experiment. *Monthly Weather Review*, 91(3):99–164, 1963.

[9] V. Springel. The cosmological simulation code GADGET-2. *MNRAS*, 364:1105–1134, 2005.

[10] C. Ulrich and T. Rung. Massively-Parallel SPH-Simulations of Viscous Flows. In *4th international SPHERIC workshop*, Nantes, France, 2009.

[11] D. J. Veen and T. P. Gourlay. SPH Study of High Speed Ship Slamming. In *3rd ERCOFTAC SPHERIC workshop on SPH applications*, 2008.